Article

Rare-earth Doped Nanoparticles with Narrow NIR-II Emission for Optical Imaging with Reduced Autofluorescence

LU Feng[1], ZHAO Ting[1], SUN Xiaojun[1], WANG Zuqiang[1], FAN Quli[1]✉ and HUANG Wei[1,2]

Received April 14, 2021
Accepted May 22, 2021

Fluorescence imaging in the second near-infrared region(900—1700 nm, NIR-II) with a high resolution and penetration depth due to the significantly reduced tissue scattering and autofluorescence has emerged as a useful tool in biomedical fields. Recently, many efforts have been devoted to the development of fluorophores with an emission band covering the long-wavelength end of NIR-II region(1500—1700 nm) to eliminate the autofluorescence. Alternatively, we believe imaging with a narrow bandwidth could also reduce the autofluorescence. As a proof of concept, $NaYF_4$:Yb,Nd@$NaYF_4$ downconversion nanoparticles(DCNPs) with sharp NIR-II emission were synthesized. The luminescence of DCNPs showed a half-peak width of 49 nm centered at 998 nm, which was perfectly matched with a (1000±25) nm bandpass filter. With this filter, we were able to retain most of the emissions from the nanoparticles, while the autofluorescence was largely reduced. After PEGylation, the DCNPs exhibited great performance for blood vessel and tumor imaging in living mice with significantly reduced autofluorescence and interference signals. This work provided an alternative way for the low-autofluorescence imaging and emphasized the importance of narrow emitting rare-earth doped nanoparticles for NIR-II imaging.

Keywords Second near-infrared; Rare-earth; Downconversion nanoparticle; Autofluorescence; Fluorescence imaging

1 Introduction

Benefiting from the real-time wide-field image acquisition and high spatial resolution, fluorescence imaging has been widely investigated over the past few decades in all kinds of biomedical fields[1—4]. For *in vivo* fluorescence imaging, the reduction of tissue autofluorescence is crucial for the improvement of imaging quality and signal-to-noise ratio[5,6]. Thus, the emission wavelength should be located in the near-infrared region(650—1700 nm) for *in vivo* imaging[7—9]. Recently, it is found that imaging in the second near-infrared(900—1700 nm, NIR-II) region can offer a much higher penetration depth and resolution comparing with traditional fluorescence imaging in the first near-infrared(700—900 nm, NIR-I) window due to the largely reduced autofluorescence and photon scattering *in vivo*[10], and thus emerges as a promising and intensely focused area. The NIR-II imaging technique even has been adopted for the imaging-guided surgical resection of liver tumors in humans[11].

Many efforts have been devoted to further reducing the tissue autofluorescence. Over the past few years, fluorophores with an emission band covering the long-wavelength end of NIR-II window(1500—1700 nm) have received great attentions, because the tissue autofluorescence in this region is negligible[12]. Indeed, fluorescence imaging in this region can provide nearly zero tissue autofluorescence and high resolution in living mice. However, the probes emitting in this region are limited. It is still difficult for organic fluorophores to reach this region[13]. For Pb-based quantum dots, their emission peaks can be easily tuned to above 1500 nm, while their stability in biological solutions and potential biotoxicity are problematic[14,15]. Besides, resulting from the serious absorption from water, *in vivo* imaging in 1500—1700 nm cannot offer a high penetration depth although the tissue autofluorescence is eliminated[16].

Alternatively, imaging with a narrow bandwidth could also reduce the background signal since the autofluorescence covers a broad range between 900 and 1500 nm in the NIR-II region. This idea requires the imaging probe to have a sharp emission band. Fortunately, rare-earth doped nanoparticles with an atomic-like spectrum can be an excellent candidate. Rare-earth based upconversion nanoparticles have been widely used for bio-imaging with a low background due to their anti-stokes emission[17]. However, upconversion nanoparticles usually emit light in the first near-infrared window[18], and thus cannot provide high resolution for *in vivo* imaging. With the rapid development of NIR-II imaging, downconversion luminescence of rare-earth doped nanoparticles has attracted lots of attentions[19]. These

✉ FAN Quli
iamqlfan@njupt.edu.cn
1. State Key Laboratory of Organic Electronics and Information Displays & Institute of Advanced Materials(IAM), Nanjing University of Posts & Telecommunications, Nanjing 210023, P. R. China;
2. Frontiers Science Center for Flexible Electronics(FSCFE), MIIT Key Laboratory of Flexible Electronics(KLoFE), Northwestern Polytechnical University, Xi'an 710072, P. R. China

downconversion nanoparticles(DCNPs) with sharp emission bands in NIR-II region can be possible solution for the low autofluorescence and high-resolution imaging after combining with a suitable bandpass filter.

Here, Yb^{3+} ions with strong emission in the NIR-II region were selected as the activator, while Nd^{3+} ions, which absorb light of around 800 nm were used as the sensitizer. After surface passivation, the Yb^{3+} and Nd^{3+} co-doped downconversion nanocrystals($NaYF_4$:Yb,Nd@$NaYF_4$) exhibited a sharp emission band in the NIR-II region, with a half-peak width of 49 nm centered at 998 nm. As shown in Fig.1, the light energy that Nd^{3+} absorbed can be transferred to Yb^{3+} ions. The energy transfer between $^4F_{3/2}$ energy level of Nd^{3+} and $^2F_{5/2}$ energy level of Yb^{3+} was very efficient according to the previous reports[20]. Meanwhile, Yb^{3+} ions with only two energy levels can provide nearly unity quantum efficiency[21]. Thus, $NaYF_4$:Yb, Nd@$NaYF_4$ nanoparticles exhibited a high NIR-II fluorescent quantum yield(QY) of 30.3% in chloroform and 18.8% in water after optimization(using IR-26 as a reference dye, QY=0.05% in dichloroethane). Combining with a (1000±25) nm bandpass filter, fluorescence emission from DCNPs can be largely retained while the autofluorescence and background signals were significantly reduced. The high penetration depth was certificated as well. After PEGylation, these DCNPs served as excellent imaging probes for blood vessel and tumor imaging. High quality NIR-II imaging with low autofluorescence and high resolution was demonstrated *in vivo*. This work demonstrated that imaging with a narrow bandwidth could also effectively reduce the autofluorescence other than imaging with a longer wavelength. Besides, NIR-II imaging at around 1000 nm could provide a much higher penetration depth comparing with imaging at 1500—1700 nm. Thus, the rare-earth doped nanoparticles with a narrow emission band and a high quantum yield can be excellent fluorophores for the fabrication of various nanoprobes for NIR-II imaging with reduced autofluorescence.

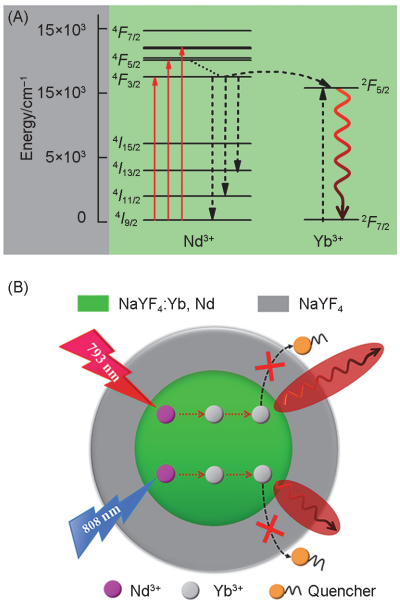

Fig.1 Schematic illustration of the energy-level diagrams(A) and energy-transfer mechanism in $NaYF_4$:Yb,Nd@$NaYF_4$ under NIR excitation(B)

2 Experimental

2.1 Materials

Rare-earth(RE)(III) acetate hydrates(RE: Y, Yb, Nd, Er) were provided by Alfa Aesar Co., Ltd., USA. NaOH, NH_4F, 1-octadecene and oleic acid were purchased from Sigma-Aldrich Co., Ltd., USA. Sodium oleate was obtained from TCI Co., Ltd., Japan. 1,2-Distearoyl-sn-glycero-3-phosphoethanolamine-*N*-methoxy(polyethylene glycol)](DSPE-PEG) was purchased from Laysan Bio, Inc., USA. IR-26 were provided by Exciton. Solvents were all supplied by Sinopharm Chemical Reagent Co., Ltd., China.

2.2 Instruments

Transmission electron microscopy(TEM) images were obtained using an HT7700 transmission electron microscope at an acceleration voltage of 100 kV. The hydrodynamic diameter and zeta potential were acquired on a Particle Size Analyzer 90Plus from Brookhaven. Absorption spectra were recorded on a UV-3600Plus spectrophotometer from Shimadzu. Photoluminescence(PL) spectra were measured on a Fluorolog 3 spectrophotometer from Horiba. Fluorescence imaging were captured with an NIRvana 640 InGaAs camera from Princeton. A bandpass filter[(1000±25) nm] was obtained from Edmundoptics, and a 900 nm longpass filter was purchased from Thorlabs.

2.3 Preparation of $NaYF_4$:Yb,Nd@$NaYF_4$ Downconversion Nanoparticles

The $NaYF_4$:Yb,Nd core was synthesized first. Typically, $Y(CH_3COO)_3$, $Nd(CH_3COO)_3$, and $Yb(CH_3COO)_3$(1 mmol in total) were added to a 100 mL flask containing 7 mL of oleic acid and 15 mL of 1-octadecene. The mixture was heated to 150 °C and maintained for 30 min under nitrogen flow to yield a transparent solution. The solution was allowed to cool to 50 °C, and then 10 mL of methanol solution containing 4 mmol of NH_4F and 2.5 mmol of sodium oleate was slowly added. After stirring for 30 min, the solution was slowly heated to 120 °C and maintained for 20 min to remove the low boiling point solvents, and the reaction solution was then heated to 290 °C under nitrogen and kept at this temperature for 90 min.

https://doi.org/10.1007/s40242-021-1172-9

The resulting solution was naturally cooled to the room temperature, and the product was collected by centrifugation after the addition of excess ethanol. After washing with ethanol twice, the core nanocrystals were dispersed in 7 mL of chloroform.

$NaYF_4$ shell was coated on the $NaYF_4$:Yb,Nd core to passivate the surface of the nanocrystals. $Y(CH_3COO)_3$ (0.5 mmol) was mixed with 7 mL of OA and 15 mL of ODE, and the mixture was heated to 150 °C to obtain a clear solution. Then 3.5 mL of $NaYF_4$:Yb,Nd and 7 mL of methanol solution containing 2 mmol of NH_4F and 1.25 mmol of NaOH were slowly added in sequence, and the mixture was stirred for 30 min. After evaporating the low-boiling solvents at 120 °C, the solution was heated to 280 °C for 1.5 h. Finally, the resulting core-shell nanocrystals were collected and purified with an identical procedure as that for the core. The obtained core-shell nanocrystals in chloroform were stored in a refrigerator at 4 °C for further characterizations.

2.4 Phase Transfer of Downconversion Nanoparticles

In order to transfer the obtained rare-earth nanoparticles into the aqueous phase, a microemulsion method was applied[22]. Briefly, 250 μL of $NaYF_4$:Yb,Nd@$NaYF_4$ nanoparticles in chloroform were first mixed with 2.5 mL of water containing 4 mmol/L DSPE-PEG under sonication. The mixture was then heated to 60—70 °C with a water bath to evaporate the chloroform, forming a transparent solution. The resulting PEGylated downconversion nanoparticles(DCNPs-PEG) were filtered through a 0.22 μm syringe filter and purified by an ultrafiltration tube(100000).

2.5 *In vivo* NIR-II Imaging with Downconversion Nanoparticles

Home-made imaging set-up equipped with an NIRvana 640 InGaAs camera was adopted to capture the NIR-II fluorescence images of the mice. The fluorescence images were acquired at different time points after the intravenous injection of DCNPs-PEG at a dose of *ca*. 15 mg/kg with a 900 nm longpass filter or a 1000 nm bandpass filter. Then 808 nm laser was used as the excitation source with a power density of *ca*. 50 mW/cm^2. All mice were obtained from Jiangsu KeyGEN BioTECH Corp., Ltd.(Nanjing, China). All animal experiments were approved by the Animal Ethics Committee of Simcere Bio Tech Co., Ltd. The obtained images were processed with the software ImageJ and the brightness/contrast was adjusted with an auto mode unless otherwise mentioned.

3 Results and Discussion

3.1 Synthesis and Optimization of $NaYF_4$:Yb,Nd@$NaYF_4$ Nanoparticles

The $NaYF_4$:Yb,Nd core with a diameter of (12.6±0.7) nm [Fig.2(A)], was prepared with a thermal decomposition approach according to the previous report[23]. After epitaxial growth of $NaYF_4$ layer on the core, the obtained $NaYF_4$:Yb,Nd@$NaYF_4$ core-shell nanoparticles grew to (17.0±1.3) nm [Fig.2(B)], demonstrating the successful shell coating. The nanoparticles can be indexed as the pure hexagonal-phase (JCPDS No.16-0334), as shown in Fig.S1(see the Electronic Supplementary Material of this paper). The absorption spectrum of these nanoparticles exhibited three characteristic peaks at around 740, 800 and 865 nm, as shown in Fig.2(C), which can be attributed to the $^4I_{9/2}\rightarrow{}^4F_{7/2}$, $^4I_{9/2}\rightarrow{}^4F_{5/2}$ and $^4I_{9/2}\rightarrow{}^4F_{3/2}$ transitions of Nd^{3+} ions[24]. As shown in Fig.1, Nd^{3+} ions were used as sensitizer to harvest light of around 800 nm, and the

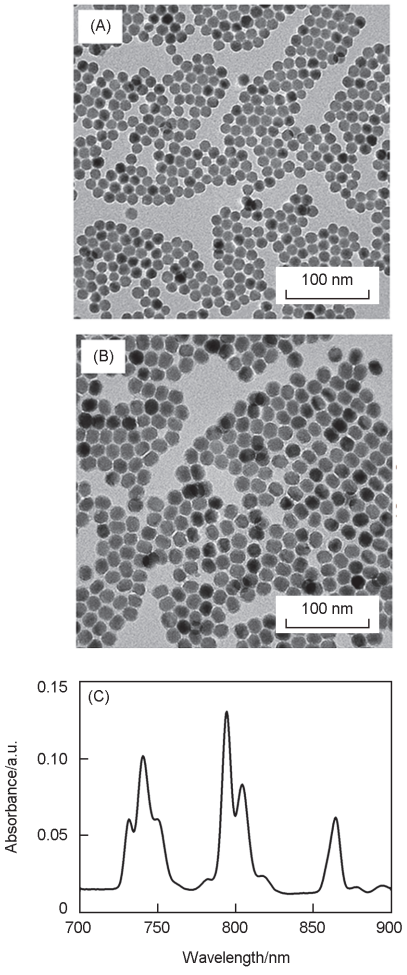

Fig.2 TEM images of $NaYF_4$:$Yb_{0.1}Nd_{0.2}$(A) and $NaYF_4$: $Yb_{0.1}Nd_{0.2}$@$NaYF_4$(B) nanocrystals, and the absorption spectrum of the core-shell nanocrystals(C)

https://doi.org/10.1007/s40242-021-1172-9

energy was then transferred to Yb^{3+} ions to emit light of around 1000 nm.

Nd^{3+} doped rare-earth nanoparticles without Yb^{3+} ions with emission peaks at 1060 and 1340 nm have been widely used for NIR-II imaging[24—26]. Thus, $NaYF_4:Nd_{0.05}$ and $NaYF_4:Nd_{0.05}@NaYF_4$ nanocrystals were prepared for comparison here(Fig.S2, see the Electronic Supplementary Material of this paper). After Yb^{3+} ions were incorporated with a concentration of 5%, $NaYF_4:Yb_{0.05},Nd_{0.05}$ nanoparticles exhibited a strong emission at around 1000 nm, while the emission intensities at 1060 and 1340 nm were decreased significantly comparing with that of the $NaYF_4:Nd_{0.05}$ nanoparticles, as shown in Fig.S3(see the Electronic Supplementary Material of this paper). Note that the emission intensity of $NaYF_4:Yb_{0.05},Nd_{0.05}$ nanoparticles was much stronger than that of $NaYF_4:Nd_{0.05}$. This trend was more obvious after $NaYF_4$ coating. The integrated emission intensity of $NaYF_4:Yb_{0.05},Nd_{0.05}@NaYF_4$ nanoparticles was about 3.9 times stronger than that of $NaYF_4:Nd_{0.05}@NaYF_4$, which indicates the high energy transfer efficiency from Nd to Yb and the high quantum efficiency of Yb^{3+} ions. Although the emission peak was slightly blue-shifted from 1060 nm to 1000 nm, this should have little influence on the imaging quality.

In order to maximize the emission intensity of the Yb, Nd co-doped nanoparticles, two series of nanoparticles with different Nd^{3+} and Yb^{3+} doping concentrations were prepared ($NaYF_4:Yb_{0.05}Nd_x$ and $NaYF_4:Yb_yNd_{0.2}$). When the doping ratio of Yb^{3+} was fixed, the emission intensity increased with the doping concentration of Nd^{3+} at the beginning and reached its maximum at 20%, as shown in Fig.3(A) and (C). Further increasing the dopant concentration led to the decrease of photoluminescence, which can be related to the severe cross-relaxation between Nd^{3+} ions at high concentrations[27]. This trend maintained after the inert shell coating, while the emission intensities were largely improved due to the surface passivation[Fig.3(B)]. Then, the doping concentration of Yb ions was optimized with a fixed Nd doping ratio at 20%[Fig.3(D) and Fig.3(E)]. The best doping ratio was 5% for the emissive core, while increased to 10%— 20% for the core-shell ones, as shown in Fig.3(F). This phenomenon indicates that the energy migration to the surface quencher played a more important role than cross-relaxation for Yb^{3+} activated nanoparticles. After the isolation of the surface quencher by $NaYF_4$ shell, a higher dopant concentration of Yb^{3+} can improve the emission intensity. Cross-relaxation was not the most important influence factor within this range(0—20%). It is important to mention that the activator concentration in lanthanide-doped materials was usually limited to less than 5%(molar ratio) to avoid deleterious cross-relaxation between dopant ions, which hindered the design of lanthanide-doped materials with enhanced brightness[28]. Here, Yb^{3+} ions as a promising activator enabled high dopant concentrations, which could be beneficial for the further fabrication of highly emissive rare-earth nanoparticles. Besides, we can find that the emission at 1000 nm was obviously higher than that of 1060 nm even if 1% Yb^{3+} were doped, which further demonstrated the high energy transfer efficiency from Nd^{3+} to Yb^{3+}. After optimization, the emission intensity of $NaYF_4:Yb_{0.1},Nd_{0.2}@NaYF_4$ nanoparticles in the NIR-II region was 6.6 times stronger than that of $NaYF_4:Nd_{0.05}@NaYF_4$, which was promising for NIR-II imaging.

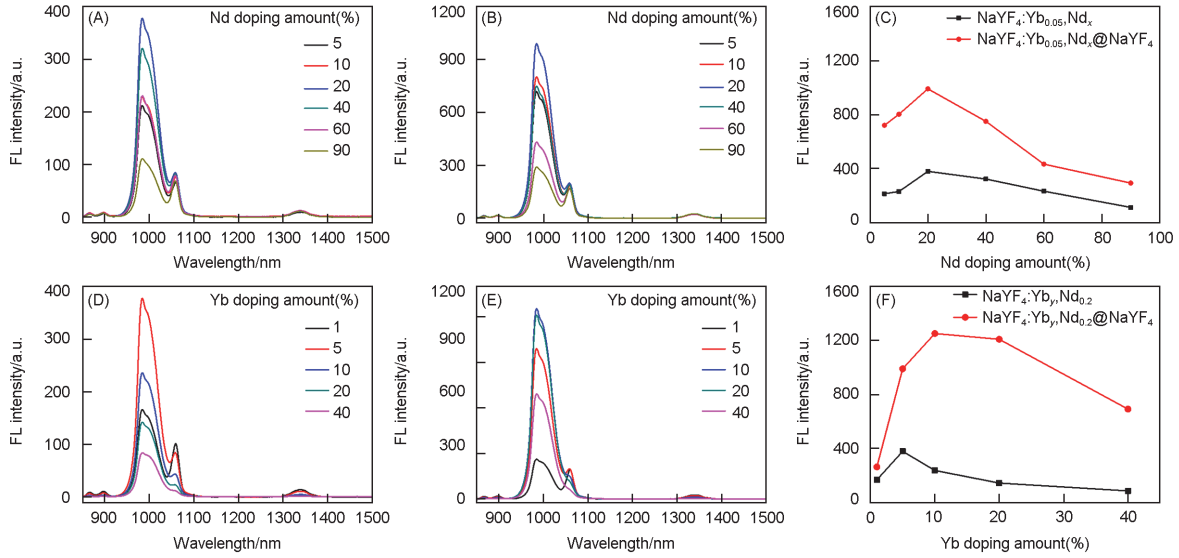

Fig.3 Emission spectra of $NaYF_4:Yb_{0.05},Nd_x$(A) and $NaYF_4:Yb_{0.05},Nd_x@NaYF_4$(B) with different Nd doping amounts, emission spectra of $NaYF_4:Yb_y,Nd_{0.2}$(D) and $NaYF_4:Yb_y,Nd_{0.2}@NaYF_4$(E) with different Yb doping amounts, and emission intensities of the corresponding core(black) and the core-shell(red) nanoparticles at 985 nm as a function of Nd(C) and Yb(F) doping ratio

https://doi.org/10.1007/s40242-021-1172-9

3.2 Optical Features of $NaYF_4$:Yb,Nd@$NaYF_4$ Nanoparticles

The absorption spectra of $NaYF_4$:Yb,Nd@$NaYF_4$ downconversion nanoparticles indicated that the 793 nm laser might be more suitable for Nd^{3+} sensitized nanomaterials than most commonly used 808 nm laser, since their absorbance at 793 nm was much higher than that at 808 nm. The fluorescence spectra in Fig.4(A) confirmed this assumption, which also coincided with the previous report[29]. These data indicated that 793 nm laser might help improve the imaging quality of Nd^{3+}-sensitized nanoparticles. The emission peak of these DCNPs showed a half-peak width of 49 nm centered at 998 nm, which could be perfectly matched with a 1000 nm bandpass filter with a 50 nm bandwidth. Thus, autofluorescence as a very broad emission can be largely reduced with this bandpass filter. As shown in Fig.4(B), the fluorescence from a mouse food pellet can be reduced to 20% with a 1000 nm bandpass filter, while the DCNPs maintain 71% of their emission. These data demonstrated the potential of Yb^{3+} activated nanoparticles for NIR-II imaging with low autofluorescence.

The penetration performance of these nanoparticles was also studied[Fig.4(C)]. $NaYF_4$:Yb,Er@$NaYF_4$ nanocrystals, which emit light of around 1530 nm under 980 nm excitation were prepared for comparison(Fig.S4, see the Electronic Supplementary Material of this paper). Their emission at around 1530 nm dropped to *ca*. 20% after passing through 2 mm water, while the emission of $NaYF_4$:$Yb_{0.1}$,$Nd_{0.2}$@$NaYF_4$ nanoparticles at 1000 nm retained 70% of its original emission after penetrating through 10 mm water, as shown in Fig.4(D). This phenomenon can be attributed to the intense absorption of water at around 1500 nm. Although fluorescence imaging with a wavelength longer than 1500 nm was considered to eliminate almost all tissue autofluorescence[12], their penetration *in vivo* may be problematic. Instead, the designed nanostructure here can provide both low autofluorescence and high penetration depth.

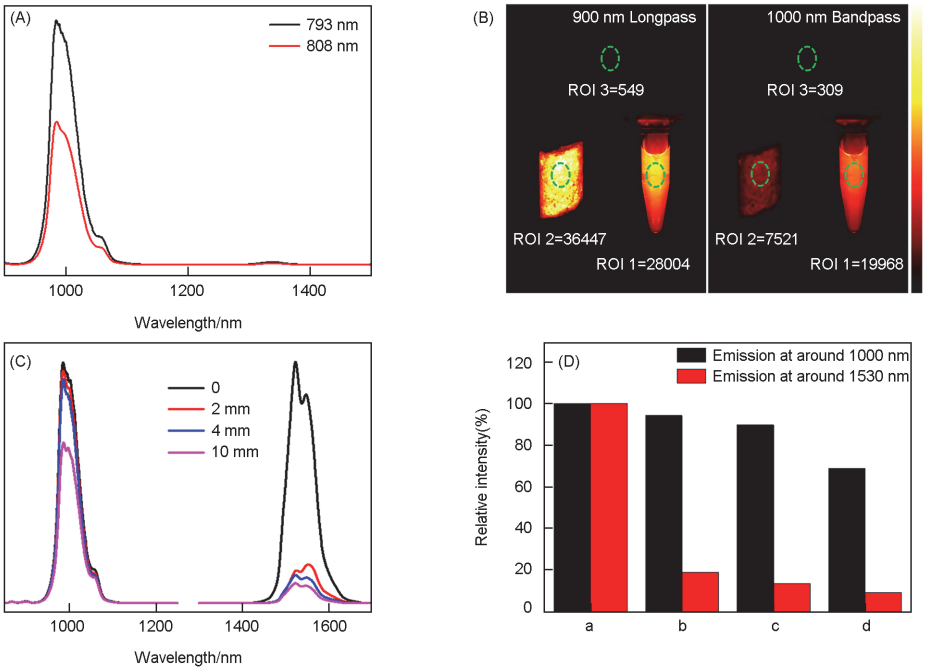

Fig.4 Emission spectra of the DCNPs under excitations with 808 nm laser(red) and 793 nm laser(black)(A), NIR-II images of a mouse food pellet and DCNPs captured with 900 nm longpass filter and 1000 nm bandpass filter(B), and emission spectra(C) and the normalized integrated emission intensities(D) of $NaYF_4$:$Yb_{0.1}$,$Nd_{0.2}$@$NaYF_4$ and $NaYF_4$:Yb,Er@$NaYF_4$ nanocrystals as a function of penetration depth in water

(D) *d*/nm: a. 0; b. 2; c. 4; d. 10.

3.3 Phase Transfer of $NaYF_4$:Yb,Nd@$NaYF_4$ Nanoparticles

The obtained nanoparticles were PEGylated and transferred into the aqueous solution for bioimaging purpose, which enables long blood circulation time and high passive targeting ability[30]. The amphipathic DSPE-PEG 5000 was coated on the surface of oleic acid capped downconversion nanoparticles through a microemulsion method. Based on the absorption spectra of the nanoparticles before and after phase transfer (Fig.S5, see the Electronic Supplementary Material of this paper), the transfer efficiency of the nanoparticles was around 97%, which showed that almost all the nanoparticles were

https://doi.org/10.1007/s40242-021-1172-9

transferred from chloroform into water. The obtained DCNPs-PEG with a zeta potential of (–10.3±2.2) mV was well dispersed in aqueous solution(Fig.S6, see the Electronic Supplementary Material of this paper), and exhibited a hydrodynamic diameter of 25.9 nm[Fig.5(A)], which was a little larger than the diameter in TEM due to the grafting of polymer layer. The emission intensity was only slightly reduced after phase transfer due to the presence of passivation layer[31], as shown in Fig.5(B). The quantum yields of these nanoparticles were characterized with a reference dye(IR-26, QY=0.05%), according to the previous report[29,32], as shown in Fig.S7(see the Electronic Supplementary Material of this paper). The QY of $NaYF_4$:$Yb_{0.1}$,$Nd_{0.2}$@$NaYF_4$ in chloroform can reach up to 30.3%. After being transferred into water, the emission intensity was decreased and the fluorescent quantum yield dropped to 18.8%. Nonetheless, this value was still much higher than those of most other fluorophores[33]. The hydrodynamic diameter of the DCNPs-PEG did not change after 7 d storage, which demonstrated the excellent colloidal stability(Fig.S8, see the Electronic Supplementary Material of this paper). The photostability was demonstrated by the irradiation of the nanoparticles with an 808 nm laser at a power density of 500 mW/cm^2. The emission intensity of DCNPs-PEG did not decrease after 1 h irradiation(Fig.S9, see the Electronic Supplementary Material of this paper), while the emission of indocyanine green was almost disappeared. MTT assay was also performed to prove the biocompatibility of the nanoparticles. The cells can retain more than 95% viability after incubating with DCNPs-PEG at a concentration of 200 μg/mL, as shown in Fig.S10(see the Electronic Supplementary Material of this paper).

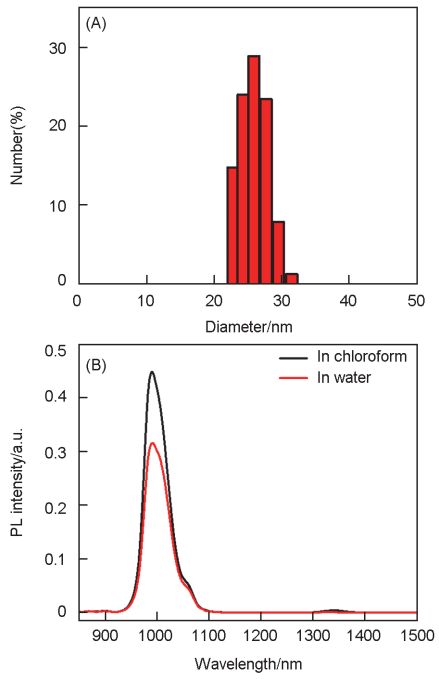

Fig.5 Hydrodynamic diameter of DCNPs after PEGylation(A) and photoluminescence spectra of oleic acid capped DCNPs in chloroform and PEGylated DCNPs in water at the same concentration(B)

3.4 *In vivo* NIR-II Imaging with PEGylated Down-conversion Nanoparticles

Encouraged by the superior fluorescent performance and good biocompatibility of the DCNPs, *in vivo* experiments were performed to demonstrate their potential for low autofluorescence bioimaging. The blood circulation of DCNPs-PEG with different PEG molecular weights were compared firstly with depilated BALB/c mice. As shown in Fig.S11(see the Electronic Supplementary Material of this paper), DCNPs modified with short PEG were excluded from blood circulation faster. Meanwhile, the emission intensity in liver retained for a longer time. Fluorescence in hindlimb vessels was completely disappeared after 4 h post-injection when the PEG molecular weight was 2000, while it can last at least 8 h when the PEG molecular weight increased to 5000(Fig.S12, see the Electronic Supplementary Material of this paper). The metabolic kinetics(Fig.S13, see the Electronic Supplementary Material of this paper) of the nanoparticles *in vivo* indicated a blood circulation time of 4.8 h. It seems that a longer PEG length enabled both long blood circulation time and fast metabolism in visceral organs, and thus DCNPs modified with DSPE-PEG at a molecular weight of 5000 were applied for further study.

The imaging qualities of whole-body blood vessels with two different filters were compared subsequently, as shown in Fig.6. No matter which filter was used, quite a number of blood vessels were clearly observed 10 min after the injection, indicating the high resolution of NIR-II imaging. When 1000 nm bandpass filter was used to reduce the autofluorescence, the blood vessels were more distinct, especially for the ones on top of the liver. Fluorescence intensity profiles along the hindlimb vessel in Fig.6 demonstrated that although the overall fluorescence intensity dropped with a bandpass filter, the decrease of the autofluorescence intensity was more significant. These observations were in accord with the *in vitro* results in Fig.4(B). Thus, DCNPs combined with a bandpass filter could reduce the autofluorescence and improve the imaging quality of blood vessel *in vivo*.

Thereafter, HeLa tumor-bearing nude mice were applied as a model for *in vivo* NIR-II tumor imaging. At 24 h post intravenous injection of DCNPs-PEG, the mice were anesthetized for NIR-II imaging. It is obvious that the nanoparticles can be accumulated at the tumor site due to the passive targeting effect(Fig.7). When a 900 nm longpass filter was used to capture all the signals in the NIR-II region, the emission in intestine was obvious. In comparison, the autofluorescence

https://doi.org/10.1007/s40242-021-1172-9

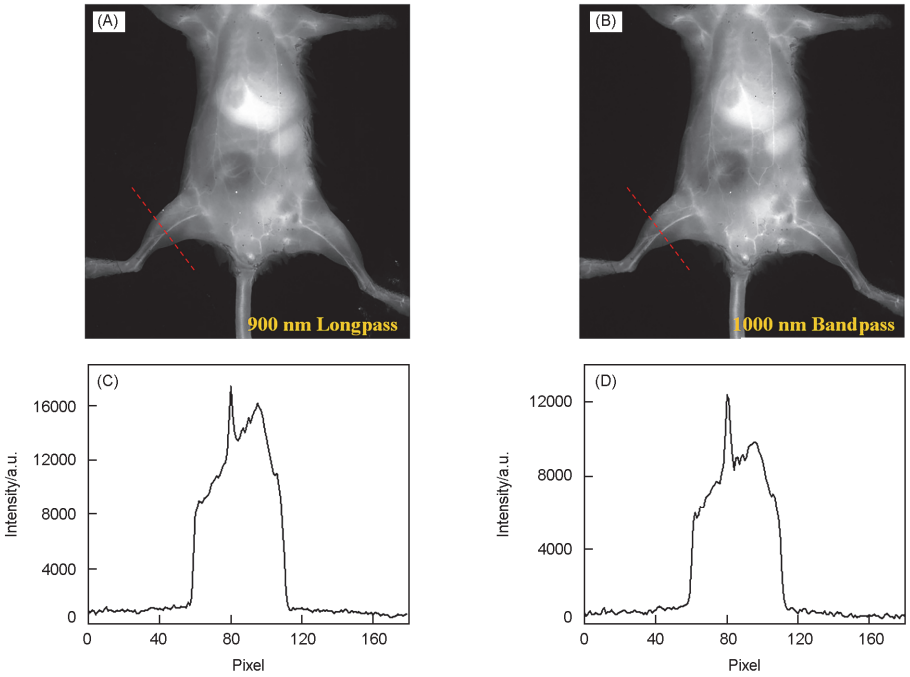

Fig.6 Images of the whole-body blood vessels(A, B) and the corresponding fluorescence intensity profiles(C, D) along the red-dashed line captured with 900 nm long pass filter(A, C) and 1000 nm bandpass filter(B, D) at around 10 min post-injection

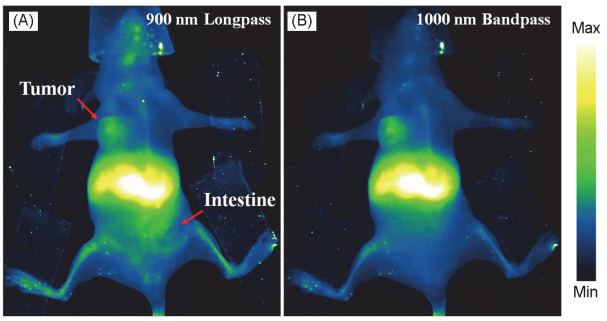

Fig.7 NIR-II fluorescence images of HeLa tumor-bearing nude mice 24 h post intravenous injection of DCNPs-PEG(*ca.* 15 mg/kg) captured with 900 nm long pass filter(A) and 1000 nm bandpass filter(B)

in abdomen and other interference signals can be largely reduced when a 1000 nm bandpass filter was applied, which can help distinguishing the tumor position. This phenomenon indicated the great potential of narrow emitting rare-earth nanoparticles for tumor imaging.

4 Conclusions

In summary, rare-earth doped nanoparticles($NaYF_4$:Yb,Nd@$NaYF_4$) with a strong emission at around 1000 nm were obtained. The doping concentrations of Yb^{3+} and Nd^{3+} ions were carefully optimized to improve their fluorescence intensity. The optimal nanoparticles exhibited an emission centered at 998 nm with a half-peak width of 49 nm, which was perfectly matched with a (1000±25) nm bandpass filter. NIR-II imaging with this bandpass filter could largely reduce the autofluorescence, while maintain most of the emission intensity from the nanoparticles. After phase transfer, the PEGylated nanoparticles maintained a high quantum yield of around 18.8% in the NIR-II region with an excellent colloidal stability in aqueous solution. The obtained PEGylated nanoparticles combined with a 1000 nm bandpass filter could offer high quality whole-body blood vessels and tumor imaging with largely reduced autofluorescence *in vivo*. The excellent imaging performance made them ideal candidates for the fabrication of a variety of NIR-II florescent probes.

Electronic Supplementary Material

Supplementary material is available in the online version of this article at http://dx.doi.org/10.1007/s40242-021-1172-9.

Acknowledgements

This work was supported by the National Natural Science Foundation of China(Nos.21975131, 21674048), the Fund of Synergetic Innovation Center for Organic Electronics and Information Displays, and the Primary Research & Development Plan of Jiangsu Province, China(No.BE2016770).

Conflicts of Interest

The authors declare no conflicts of interest.

References

[1] Hong G. S., Antaris A. L., Dai H. J., *Nat. Biomed. Eng.*, **2017**, *1*, 0010
[2] Ding F., Feng J., Zhang X., Sun J., Fan C., Ge Z., *Adv. Drug. Deliv. Rev.*, **2021**, *173*, 141
[3] Cheng H. B., Li Y. Y., Tang B. Z., Yoon J., *Chem. Soc. Rev.*, **2020**, *49*, 21
[4] Chen C., Ni X., Tian H. W., Liu Q., Guo D. S., Ding D., *Angew. Chem. Int.*

Ed., **2020**, *59*, 10008
[5] Feng G. X., Zhang G. Q., Ding D., *Chem. Soc. Rev.*, **2020**, *49*, 8179
[6] Ni X., Zhang X. Y., Duan X. C., Zheng H. L., Xue X. S., Ding D., *Nano Lett.*, **2019**, *19*, 318
[7] Tang Y. F., Pei F., Lu X. M., Fan Q. L., Huang W., *Adv. Opt. Mater.*, **2019**, *7*, 1900917
[8] Liu W., Zhang Y. H., Qi J., Qian J., Tang B. Z., *Chem. Res. Chinese Universities*, **2021**, *37*(1), 171
[9] Zhang L. P., Che W. L., Yang Z. Y., Liu X. M., Liu S., Xie Z. G., Zhu D. X., Su Z. M., Tang B., Bryce M. R., *Chem. Sci.*, **2020**, *11*, 2369
[10] Yang H. C., Li R. F., Zhang Y. J., Yu M. X., Wang Z., Liu X., You W. W., Tu D. T., Sun Z. Q., Zhang R., Chen X. Y., Wang Q. B., *J. Am. Chem. Soc.*, **2021**, *143*, 2601
[11] Hu Z. H., Fang C., Li B., Zhang Z. Y., Cao C. G., Cai M. S., Su S., Sun X. W., Shi X. J., Li C., Zhou T. J., Zhang Y. X., Chi C. W., He P., Xia X. M., Chen Y., Gambhir S. S., Cheng Z., Tian J., *Nat. Biomed. Eng.*, **2020**, *4*, 259
[12] Diao S., Hong G. S., Antaris A. L., Blackburn J. L., Cheng K., Cheng Z., Dai H. J., *Nano Res.*, **2015**, *8*, 3027
[13] Li J., Liu Y., Xu Y. L., Li L., Sun Y., Huang W., *Coord. Chem. Rev.*, **2020**, *415*, 213318
[14] Zebibula A., Alifu N., Xia L. Q., Sun C. W., Yu X. M., Xue D. W., Liu L. W., Li G. H., Qian J., *Adv. Funct. Mater.*, **2018**, *28*, 1703451
[15] Yu W. W., Falkner J. C., Shih B. S., Colvin V. L., *Chem. Mater.*, **2004**, *16*, 3318
[16] Cui J. B., Jiang R., Guo C., Bai X. L., Xu S. Y., Wang L. Y., *J. Am. Chem. Soc.*, **2018**, *140*, 5890
[17] Zheng K. Z., Loh K. Y., Wang Y., Chen Q. S., Fan J. Y., Jung T., Nam S. H., Suh Y. D., Liu X. G., *Nano Today*, **2019**, *29*, 100797
[18] Chhetri B. P., Karmakar A., Ghosh A., *Part. Part. Syst. Charact.*, **2019**, *36*, 1900153
[19] Zhong Y. T., Dai H. J., *Nano Res.*, **2020**, *13*, 1281
[20] Liegard F., Doualan J. L., Moncorge R., Bettinelli M., *Appl. Phys. B: Lasers O*, **2005**, *80*, 985
[21] Gu Y. Y., Guo Z. Y., Yuan W., Kong M. Y., Liu Y. L., Liu Y. T., Gao Y. L., Feng W., Wang F., Zhou J. J., Jin D. Y., Li F. Y., *Nat. Photonics*, **2019**, *13*, 580
[22] Wang Y. X., Feng L. H., Wang S., *Adv. Funct. Mater.*, **2019**, *29*, 1806818
[23] Lu F., Yang L., Ding Y. J., Zhu J. J., *Adv. Funct. Mater.*, **2016**, *26*, 4778
[24] Villa I., Vedda A., Cantarelli I. X., Pedroni M., Piccinelli F., Bettinelli M., Speghini A., Quintanilla M., Vetrone F., Rocha U., Jacinto C., Carrasco E., Rodriguez F. S., Juarranz A., del Rosal B., Ortgies D. H., Gonzalez P. H., Sole J. G., Garcia D. J., *Nano Res.*, **2015**, *8*, 649
[25] Wang R., Zhou L., Wang W. X., Li X. M., Zhang F., *Nat. Commun.*, **2017**, *8*, 14702
[26] Wang P. Y., Fan Y., Lu L. F., Liu L., Fan L. L., Zhao M. Y., Xie Y., Xu C. J., Zhang F., *Nat. Commun.*, **2018**, *9*, 2898
[27] Cao C., Xue M., Zhu X. J., Yang P. Y., Feng W., Li F. Y., *ACS Appl. Mat. Interfaces*, **2017**, *9*, 18540
[28] Johnson N. J., He S., Diao S., Chan E. M., Dai H., Almutairi A., *J. Am. Chem. Soc.*, **2017**, *139*, 3275
[29] Ding L. H., Ren F., Liu Z., Jiang Z. L., Yun B. F., Sun Q., Li Z., *Bioconjugate Chem.*, **2020**, *31*, 340
[30] Lu F., Doane T. L., Zhu J. J., Burda C., *Chem. Commun.*, **2014**, *50*, 642
[31] Zhong Y. T., Ma Z. R., Zhu S. J., Yue J. Y., Zhang M. X., Antaris A. L., Yuan J., Cui R., Wan H., Zhou Y., Wang W. Z., Huang N. F., Luo J., Hu Z. Y., Dai H. J., *Nat. Commun.*, **2017**, *8*, 737
[32] Cosco E. D., Caram J. R., Bruns O. T., Franke D., Day R. A., Farr E. P., Bawendi M. G., Sletten E. M., *Angew. Chem. Int. Ed.*, **2017**, *56*, 13126
[33] Yang Y. Q., Fan X. X., Li L., Yang Y. M., Nuernisha A., Xue D. W., He C., Qian J., Hu Q. L., Chen H., Liu J., Huang W., *ACS Nano*, **2020**, *14*, 2509